



Aalborg Universitet

AALBORG UNIVERSITY  
DENMARK

## Cost-Effective DC Current Suppression for Single-Phase Grid-Connected PV Inverter

Guo, Bin; Su, Mei; Sun, Yao; Wang, Hui; Li, Xing; Liao, Yuefeng; Lin, Jianheng; Yang, Y.

*Published in:*

IEEE Journal of Emerging and Selected Topics in Power Electronics

*DOI (link to publication from Publisher):*

[10.1109/JESTPE.2020.3029393](https://doi.org/10.1109/JESTPE.2020.3029393)

*Publication date:*

2021

*Document Version*

Accepted author manuscript, peer reviewed version

[Link to publication from Aalborg University](#)

*Citation for published version (APA):*

Guo, B., Su, M., Sun, Y., Wang, H., Li, X., Liao, Y., Lin, J., & Yang, Y. (2021). Cost-Effective DC Current Suppression for Single-Phase Grid-Connected PV Inverter. *IEEE Journal of Emerging and Selected Topics in Power Electronics*, 9(2), 1808-1823. Article 9216014. <https://doi.org/10.1109/JESTPE.2020.3029393>

### General rights

Copyright and moral rights for the publications made accessible in the public portal are retained by the authors and/or other copyright owners and it is a condition of accessing publications that users recognise and abide by the legal requirements associated with these rights.

- Users may download and print one copy of any publication from the public portal for the purpose of private study or research.
- You may not further distribute the material or use it for any profit-making activity or commercial gain
- You may freely distribute the URL identifying the publication in the public portal -

### Take down policy

If you believe that this document breaches copyright please contact us at [vbn@aub.aau.dk](mailto:vbn@aub.aau.dk) providing details, and we will remove access to the work immediately and investigate your claim.

# Cost-Effective DC Current Suppression for Single-Phase Grid-Connected PV Inverter

Bin Guo, Mei Su, Yao Sun, *Member, IEEE*, Hui Wang, Xing Li, Yuefeng Liao, *Student Member, IEEE*, Jianheng Lin, and Yongheng Yang, *Senior Member, IEEE*

**Abstract**—Due to the disparity of power modules, asymmetry of driving pulses and measurement errors of sensors, dc currents may be injected to grid-connected photovoltaic (PV) inverters. The dc current injection may cause magnetic saturation of the power transformers. To solve this issue, this paper thus proposes an effective current control strategy and compensation method, which does not require any extra sensor and hardware circuit. Firstly, the root-cause of dc current injection is comprehensively analyzed. Subsequently, a proportional-integral-resonant (PIR) controller is proposed to eliminate the dc component caused by disparity of power modules, asymmetry of driving pulses and measurement errors of grid voltage. The injected dc current caused by grid current measurement error is estimated from the line-frequency ripple of the dc-link voltage and then it is suppressed by a feedback compensation controller. In addition, the dc current rejection capability is evaluated and the proposed method is benchmarked with the virtual capacitor-based method. Finally, experimental tests are performed on a 1.2-kW single-phase PV inverter to verify the effectiveness of the proposal.

**Index Terms**—Photovoltaic (PV) systems, grid-connected inverter, dc current injection, transformer saturation, PIR current controller.

## I. INTRODUCTION

DUe to the merits of high efficiency, low cost and small size, transformerless grid-connected inverters have become more and more attractive in photovoltaic (PV) systems [1], [2]. Despite the gained advantages from the transformerless structure, it may lead to several technical and safety issues, e.g., galvanic non-isolation, ground fault current, leakage current, dc current injection and voltage-level mismatch between the solar panel and grid [3], [4]. As one of the major issues, the dc current injection may result in saturation of the distribution transformers, increase system losses, cause fast corrosion of the

grounding wires and degrade power quality [5]. Consequently, several standards have been established to limit the dc current injection from PV inverter into the grid [6]–[8].

To suppress or mitigate dc current injection, many attempts have been made. They are broadly grouped into two categories: a) passive methods and b) active hardware or software techniques. The main idea of passive methods is to introduce a capacitor in the injected current path, which makes the system inherently free of dc current injection. For instance, in [9], a dc capacitor instead of an ac capacitor was serially connected between the inverter and the grid to block the dc component, where a method to prevent the capacitor from reverse polarity connection was used. However, it requires an expensive and bulky capacitor that has a low reactance at the line-frequency to effectively block the dc currents. An alternative is to use a two or three-level half-bridge inverter which utilizes the dc-link capacitor to block the dc currents [10], [11]. However, the low utilization rate of the dc-link voltage and large volume of capacitor hinder its wide application.

Regarding active methods, the auto-calibrating dc-link current sensing technique is effective to compensate for the dc component caused by the dc offset of the current measurement [12]. However, this method is not suitable for the case if the dc current is induced by other sources like the grid voltage measurement error and asymmetry of driving pulses [13]. Furthermore, to enhance the mitigation of dc current injection, many dc component measurement schemes combined with control methods have been proposed in the literature. In [14] and [15], a small 1:1 voltage transformer and an RC circuit were used to detect the dc voltage at the inverter output of an H-bridge inverter, and then the dc offset was fed back to a compensation loop. However, it is difficult to extract the dc voltage component when the inverter system operates with non-unity power factor. In addition, the impact caused by grid side bias cannot be eliminated either. Ref [16] introduced a two-stage RC filter to detect the dc component by measuring the dc voltage on the filter inductor. However, the detected result may be disturbed by noise, as the dc offset of the grid current and the series equivalent resistance of the filter inductor is small. Ref [17] and [18] develop nonlinear reactors to detect the dc voltage component at the converter output. Despite its precise dc bias measurement, the reactors should be specifically designed, which increases the system complexity. Similarly, to detect the dc component at the inverter output, the authors in [6] and [19] utilized a voltage sensor combined with a differential amplifier and a low pass filter for single-phase and three-phase systems. However, the step-down offset voltage from the differential amplifier introduces accurate measurement challenges [20]. To directly measure the grid current dc component, a coupled -inductor-based technique was presented

Manuscript received October 09, 2019; revised June 18, 2020 and August 27, 2020; accepted September 27, 2020. This work was supported in part by the National Key R&D Program of China under Grant 2018YFB0606005, in part by the National Natural Science Foundation of China under Grant 61873289 and 61933011, in part by the Project of Innovation-driven Plan in Central South University under Grant 2019CX003, in part by the Major Project of Changzhutan Self-dependent Innovation Demonstration Area under Grant 2018XK2002 and in part by the Hunan Provincial Innovation Foundation for Postgraduate under Grant CX20190122. (*Corresponding author: Yao Sun.*)

B. Guo, M. Su, Y. Sun, H. Wang, Y. F. Liao and J. H. Lin are with the School of Automation, Central South University, Changsha 410083, China (e-mail: binguo\_mail@csu.edu.cn; sumeicsu@mail.csu.edu.cn; yaosuncsu@gmail.com; wanghuicp9@csu.edu.cn; liaoyuefeng\_uav@126.com; mlrtortoise@163.com).

X. Li is with the College of Electrical and Information Engineering, Hunan University, Changsha, 410082, China (e-mail: lxhnu@hnu.edu.cn).

Y. H. Yang is with the Department of Energy Technology, Aalborg University, Aalborg, Denmark. (e-mail: yoy@et.aau.dk).

in [21], where the dc current was obtained by using a coupled-inductor and a small-range high accuracy Hall current sensor. Although this technique is effective, the use of an extra high accuracy Hall current sensor increases the overall cost.

Different from the aforementioned active hardware dc suppression schemes, the active software techniques that utilize the existing measurement signals to obtain the dc component and then feed it back to a controller are more cost-effective. Ref [22] introduced an enhanced current control scheme to eliminate the dc offset current caused by voltage measurement error. However, this current control method is not suitable for the dc component caused by other sources. In [13], [23] and [24], a virtual capacitor scheme was proposed for single and three-phase PV inverters. It replaces the physical capacitor by integrating the grid current to block the dc component in ac side. To increase the accuracy of dc component extraction, a sliding window double iteration method was proposed in [25]. After the dc component is obtained, a neural network based proportional-integral-differential (PID) controller is used in the compensation loop to eliminate the dc component. Moreover, in [20], a method to suppress dc injection was proposed, where the dc component was extracted from the dc-link current and then mitigated via a control loop. To reduce the requirement of the current sensor, the dc-link current was reconstructed by the grid current. Although the solutions in [13], [20], [23]-[25] directly extract or suppress the dc component from the grid current and do not need extra sensors, the dc component caused by the nonlinearity and offset drifts in current transducers and sampling circuits cannot be eliminated. The reasons are as follows: 1) Hall-effect sensors are usually adopted to measure the grid current. However, due to the remanence, a dc bias will be introduced into the control system [26]; 2) According to the control theory, the dc bias caused by current sensors and sampling circuits is in the controller feedback channel, and thus, it is difficult to eliminate it only using the current feedback control. To solve this issue, a compensation scheme for current and voltage measurement errors in three and single-phase grid-connected inverters was proposed in [27] and [28], where the dc-link voltage ripple combined with a low-pass filter or mean average filter was used to suppress the dc component. More specifically, in [27], the dc offset and scaling error in grid current measurement were estimated by extracting the line-frequency and double-line-frequency voltage ripples in three-phase systems. Thus, the dc offset and scaling error in current measurement can be corrected in real time, but the estimation is quite challenging, as the two variables are very small in practice. Moreover, this method cannot be applied to single-phase system due to its inherent double-line-frequency ripple in the dc-link voltage. In [28], a dc current injection compensation scheme was proposed for a current transformer (CT) sensed static synchronous compensator (STATCOM), where the impact of CT on system and the effectiveness of the proposed dc current injection elimination method have been analyzed. Despite its capability of dc current injection suppressing, the presented method still has two limitations. First, the impact of disparity of power modules and asymmetry of driving pulses on grid current offset has not been considered. Second, the root and impact of dc current injection on the inverter system have not been fully investigated and analyzed.

In light of the above, for single-phase transformerless

grid-connected PV inverters, this paper proposes a simple and effective scheme to mitigate the dc current caused by all sources without any extra sensor and hardware circuit. First, the root-causes of dc current injection and its impact on the inverter performance are thoroughly analyzed. The analysis reveals that the dc current caused by the disparity of power modules, asymmetry of driving pulses and grid voltage measurement errors can be mitigated by increasing the low-frequency gain of the current loop, while it does not work for the dc component induced by the current measurement errors. In addition, it has been further revealed that the dc current injected into the grid will result in line-frequency ripples on the dc-link voltage. Accordingly, a simple but effective proportional integral resonant (PIR) method and dc current compensation scheme are proposed. The PIR control can increase the low frequency gain, while the injected dc current due to the grid current measurement errors is estimated using the line-frequency ripple of the dc-link voltage. It is then eliminated by an extra compensation loop. Notably, the proposed compensation scheme can also be regarded as a hardware method. Compared with tradition hardware methods, e.g., by measuring inverter output voltage [6], [14], [15], [19], grid current [21] and dc-link current [20], the difference is that, as the dc-link voltage is usually measured in the PV system control, no extra sensors and hardware circuits are needed in the proposed method. Therefore, the impact of the proposed compensation method on the system stability and its control complexity are almost the same as the traditional hardware methods. The main contributions of this paper are summarized as:

- 1) The root-causes of the dc current injection and its impact on the system are analyzed in detail.
- 2) A cost-effective current control and compensation method is proposed to suppress the dc current injection without any extra sensors and hardware circuits, thus, maintaining the overall cost of the PV system.
- 3) Design guidelines for the proposed strategy are presented in detail and its dc injection rejection capability is evaluated, enabling its wide application.

The rest of this paper is organized as follows. In Section II, the root causes of the dc current injection and its impact on systems are analyzed. The proposed current control scheme is then detailed in Section III, followed by the proposed compensation method. Experimental tests are performed on a 1.2-kW single-stage single-phase PV inverter. The results are provided in Section V, where the proposed method is also benchmarked with prior-art solutions. Finally, concluding remarks are provided in Section VI.

## II. DC INJECTION ANALYSIS

### A. System Configuration and Modeling

The circuit configuration and a typical cascaded control structure of the studied single-phase transformerless PV grid-connected system are shown in Fig. 1. The PV grid-connected system is built with a single-stage highly efficient and reliable inverter concept (HERIC) to realize the dc/ac inversion, maximum power point tracking (MPPT) and transfer the power derived from the solar array to the grid. The

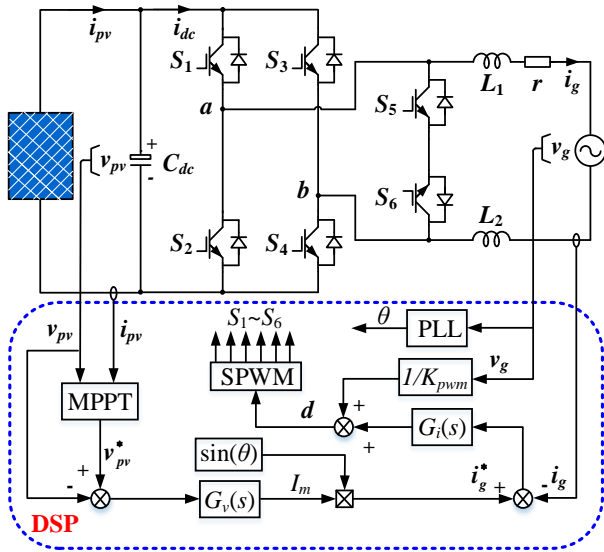


Fig. 1. System schematics and control diagrams of a single-phase transformerless grid-connected PV system ( $L_1=L_2$ , MPPT is maximum power point tracking, PLL is phase locked loop, SPWM is sinusoidal pulse width modulation, DSP is digital signal processor).

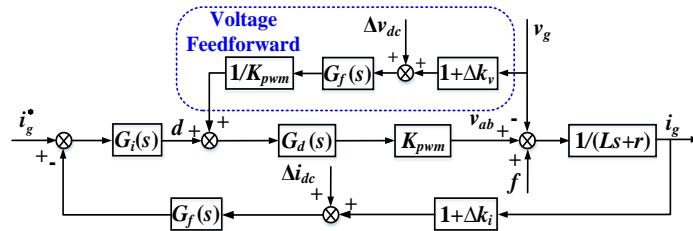


Fig. 2. Detailed control block diagram of the current loop.

main role of the two auxiliary switches  $S_5$  and  $S_6$  of the HERIC is to suppress leakage currents [29]. Considering the electromagnetic interference (EMI) filter and the grid line impedance in the practical inverter system, the ac filter is a  $LCL$  configuration. However, as the inverter is connected with an ideal programmable ac source and no EMI filters are considered in this study, for simplicity, the  $L$ -type ( $L_1 = L_2$ ) filter is adopted instead of an  $LCL$  filter to demonstrate the proposed dc current injection suppression strategy.

According to Fig. 1, the single-phase grid-connected PV inverter can be modeled as

$$C_{dc} \frac{dv_{pv}}{dt} = i_{pv} - i_{dc} \quad (1)$$

$$L \frac{di_g}{dt} = v_{ab} - ri_g - v_g \quad (2)$$

where  $L=L_1+L_2$  with  $r$  being the total series equivalent resistance of the filter inductors,  $i_{dc}$  is the dc-link current,  $v_{pv}$  and  $i_{pv}$  are the PV output voltage (dc-link voltage) and current, respectively,  $v_g$  and  $i_g$  are the grid voltage and current, respectively.

In order to control this PV grid-connected system, a typical cascaded control, as shown in Fig. 1, is presented, where  $v_{pv}^*$  is the voltage reference generated by the MPPT algorithm;  $G_v(s)$  is voltage loop regulator;  $G_i(s)$  is the current loop regulator;  $K_{pwm}$  is the gain of PWM modulator. The grid voltage feedforward is usually added into the current loop to suppress the background harmonics and disturbances of grid voltage.

## B. Root-Causes of the DC Current Injection

In order to explore the mechanism of the dc current injection and its impact on the system performance, the actual current loop control block diagram is shown in Fig. 2, where  $G_f(s) \approx 1/(T_f s + 1)$  is the sampling delay caused by filter in conditioning circuit and  $T_f$  being its time constant;  $G_d(s) \approx e^{-1.5T_s s} \approx 1/(1.5T_s s + 1)$  is the total control delay in the digital control system, including the analog to digital conversion (ADC) delay, computation delay and pulse width modulation (PWM) delay with  $T_s$  being the sampling period;  $\Delta i_{dc}$  and  $\Delta k_i$  are the dc offset and scaling error in the grid current measurement, respectively;  $\Delta v_{dc}$  and  $\Delta k_v$  are the dc offset and scaling error in the grid voltage measurement;  $f$  represents the disturbance caused by disparity of power modules and asymmetry of driving pulse, and others. Ideally, if the current, voltage sensors and the conditioning circuit are accurate enough, driving pulses are symmetrical and there is no disparity in power modules, the dc offset  $\Delta i_{dc}$ ,  $\Delta v_{dc}$ , the scaling error  $\Delta k_i$  and  $\Delta k_v$  and disturbance  $f$  will be zero.

According to Fig. 2, the closed-loop transfer function of the grid current in the  $s$ -domain is derived as

$$i_g(s) = G_{c-ig}(s)i_g^* + G_{c-\Delta i_{dc}}(s)\Delta i_{dc} + G_{c-vg}(s)v_g + G_{c-\Delta v_{dc}}(s)\Delta v_{dc} + G_{c-f}(s)f \quad (3)$$

where  $G_{c-ig}(s)$ ,  $G_{c-\Delta i_{dc}}(s)$ ,  $G_{c-vg}(s)$ ,  $G_{c-\Delta v_{dc}}(s)$  and  $G_{c-f}(s)$  are the closed-loop transfer function from the current reference  $i_g^*$ , dc offset of the grid current  $\Delta i_{dc}$ , grid voltage  $v_g$ , dc offset of the grid voltage and disturbance to the grid current  $i_g$ , respectively. They are defined as

$$G_{c-ig}(s) = \frac{i_g(s)}{i_g^*(s)} = \frac{G_i(s)G_d(s)K_{pwm}}{Ls + r + G_i(s)G_d(s)G_f(s)K_{pwm}(1 + \Delta k_i)} \quad (4)$$

$$G_{c-\Delta i_{dc}}(s) = \frac{i_g(s)}{-\Delta i_{dc}(s)} = \frac{G_i(s)G_d(s)G_f(s)K_{pwm}}{Ls + r + G_i(s)G_d(s)G_f(s)K_{pwm}(1 + \Delta k_i)} \quad (5)$$

$$G_{c-vg}(s) = \frac{i_g(s)}{v_g(s)} = \frac{(1 + \Delta k_v)G_d(s)G_f(s) - 1}{Ls + r + G_i(s)G_d(s)G_f(s)K_{pwm}(1 + \Delta k_i)} \quad (6)$$

$$G_{c-\Delta v_{dc}}(s) = \frac{i_g(s)}{\Delta v_{dc}(s)} = \frac{G_d(s)G_f(s)}{Ls + r + G_i(s)G_d(s)G_f(s)K_{pwm}(1 + \Delta k_i)} \quad (7)$$

$$G_{c-f}(s) = \frac{i_g(s)}{f(s)} = \frac{1}{Ls + r + G_i(s)G_d(s)G_f(s)K_{pwm}(1 + \Delta k_i)} \quad (8)$$

From (4)-(8), it can be seen that due to the digital and sampling delays in the control system, the dc offset in the grid voltage measurement results in dc component in the grid current. What's more, the background harmonics and disturbances of the grid voltage cannot be fully suppressed by the voltage feedforward method. To realize the zero steady-state error tracking of the grid current, a PR controller is usually adopted in the current loop [30]. Its transfer function in the  $s$ -domain is given as

$$G_{PR}(s) = k_p + \frac{2k_r \omega_c s}{s^2 + 2\omega_c s + \omega_c^2} \quad (9)$$

where  $k_p$  and  $k_r$  are the proportional and resonant gain, respectively.  $\omega_c$  is the cutoff frequency of the resonant

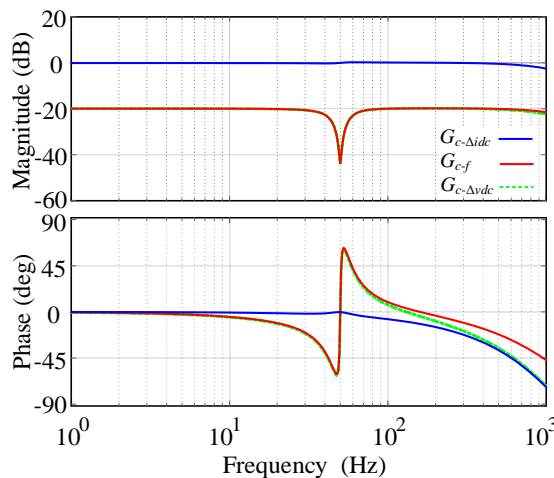


Fig.3. Bode diagram of  $G_{c-\Delta idc}(s)$ ,  $G_{c-\Delta vdc}(s)$  and  $G_{c-f}(s)$  with the scaling factor of the grid current and voltage measurement being 1.

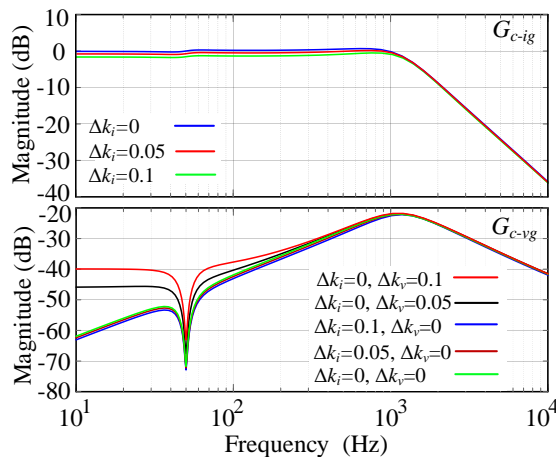


Fig.4. Bode diagram of  $G_{c-ig}(s)$ ,  $G_{c-vg}(s)$  with different grid voltage and current measurement scaling factors.

controller, and  $\omega_0$  is the fundamental angular frequency of the grid voltage.

The magnitudes of  $G_{c-\Delta idc}(s)$ ,  $G_{c-\Delta vdc}(s)$ , and  $G_{c-f}(s)$  at the frequency of 0 Hz correspondingly decide the dc injection rejection capability. Thus, the dc injection caused by disturbances, grid voltage and current dc offset measurement are given as

$$I_{dc-\Delta idc} = \Delta i_{dc} G_{c-\Delta idc}(s) |_{s=j2\pi 0} \approx \frac{\Delta i_{dc}}{1 + \Delta k_i} \quad (10)$$

$$I_{dc-\Delta vdc} = \Delta v_{dc} G_{c-\Delta vdc}(s) |_{s=j2\pi 0} \approx \frac{\Delta v_{dc}}{k_p (1 + \Delta k_i) K_{pwm}} \quad (11)$$

$$I_{dc-f} = f G_{c-f}(s) |_{s=j2\pi 0} \approx \frac{f}{k_p (1 + \Delta k_i) K_{pwm}} \quad (12)$$

According to (10)-(12), it can be seen that the scaling error of the grid current measurements will amplify the dc component if its value is negative. Although increasing the proportional gain of the PR controller contributes to the reduction of the dc component caused by disturbances and dc offset in grid voltage measurement, a large gain may affect the system stability. Fig. 3 shows the Bode diagram of  $G_{c-\Delta idc}(s)$ ,  $G_{c-f}(s)$ ,  $G_{c-\Delta vdc}(s)$  in the case of the scaling errors in the grid current and voltage measurement being zero. The parameters of PR controller designed in [31] are adopted here and the parameters of the

entire system are listed in Table I. From Fig. 3, it is indicated that  $G_{c-\Delta idc}(s)$  produces a unity gain (0 dB) at 0 Hz, which means that the dc component caused by the dc offset in the grid current measurement cannot be suppressed by the current controller. In addition, the gain of  $G_{c-f}(s)$  and  $G_{c-\Delta vdc}(s)$  at 0 Hz is -20 dB, which is not sufficient to effectively suppress the dc component caused by disturbances and dc offset in the grid voltage measurement. In addition, Fig. 4 shows the Bode diagram of  $G_{c-ig}(s)$  and  $G_{c-vg}(s)$  with different grid current and voltage measurement scaling errors. Observations from Fig. 4 indicate that the scaling error of the grid current measurement will lead to current tracking errors, but it has negligible effect on the grid voltage disturbance suppression. While, the scaling error in the grid voltage measurement will reduce the capability to attenuate the low frequency harmonics of the grid voltage.

### C. DC-Link Voltage Line-Frequency Ripple Analysis

Rewriting (1) as

$$\frac{1}{2} C_{dc} \frac{dv_{pv}^2}{dt} = v_{pv} i_{pv} - v_{pv} i_{dc} \quad (13)$$

When neglecting the power losses of the system and the small instantaneous power of the filter inductor, (13) is rewritten as

$$\frac{1}{2} C_{dc} \frac{dv_{pv}^2}{dt} = v_{pv} i_{pv} - v_g i_g \quad (14)$$

Assuming that the grid voltage is ideally sinusoidal and the grid current has a dc component  $I_{DC}$ , that is, the grid voltage and current are expressed as

$$v_g = V_m \sin(\omega_0 t) \quad (15)$$

$$i_g = I_m \sin(\omega_0 t + \varphi_i) + I_{DC} \quad (16)$$

where  $V_m$  and  $\omega_0$  are the amplitude and angular frequency of the grid voltage, respectively;  $I_m$  is the amplitude of the grid current, and  $\varphi_i$  is the phase angle of the grid current referring to the grid voltage phase. Substituting (15) and (16) into (14), and considering unity power factor operation, we have

$$C_{dc} \frac{dv_{pv}^2}{dt} = 2P_{pv} - V_m I_m + V_m I_m \cos(2\omega_0 t) - \underbrace{2I_{DC} V_m \sin(\omega_0 t)}_{P_{f0}} \quad (17)$$

where  $P_{pv} = v_{pv} i_{pv}$  is the PV output power and  $P_{f0}$  is the line-frequency power caused by dc current injection.

From (17), it can be seen that the dc-link voltage will naturally include the line-frequency ripple if the grid current has a dc component. In addition, it should be noticed that, in PV system, as the PV output power is always oscillating with the dc-link voltage ripple, it will inevitably contain line-frequency power oscillations. This will in turn affect the line-frequency ripple on the dc-link voltage. However, through analysis (shown in the Appendix I and according to (17)), it can be found that the grid current dc component is the dominant or even the only cause for the dc-link voltage line-frequency ripple. What's more, compared with the line-frequency power caused by dc current injection i.e.,  $P_{f0}$ , the line-frequency power in  $P_{pv}$  is much smaller. Thus, in this paper, the oscillation of PV output power is neglected thereafter for simplicity.

Based on the above analysis, the impact of the disturbances, dc offset and scaling error in the grid voltage and current measurements on the entire inverter system can be summarized

as follows. 1) The dc component caused by the dc offset of current measurements cannot be mitigated by the current controller. By contrast, increasing the low frequency gain of the current controller benefits to reduce the dc component produced by the dc offset of the voltage measurement and disturbances. 2) The dc current injected into the grid will produce a line-frequency ripple on the dc-link voltage, which in turn will lead to 2nd-order harmonics in the grid current. Moreover, negative scaling errors in the grid current measurement will worsen the dc injection issue, and thus increasing the dc-link voltage line-frequency ripple.

### III. PROPOSED CURRENT CONTROL SCHEME

#### A. Current Controller Design

As analyzed in Section II, the scaling error in the grid voltage measurement will lower the capability to suppress low frequency harmonics of the grid voltage. What's more, the dc component caused by disturbance and dc offsets in the grid voltage measurement can be suppressed by properly designing the current controller. Therefore, to eliminate the influence of the grid voltage measurement scaling errors on the system and to suppress dc component caused by the dc offset of the grid voltage measurement and disturbances, a PIR current controller is employed, which can be expressed as

$$G_i(s) = k_p + \underbrace{\frac{k_i}{s}}_{\text{PI}} + \underbrace{\frac{2k_r\omega_c s}{s^2 + 2\omega_c s + \omega_0^2}}_{\text{R}} \quad (18)$$

where  $k_i$  is the integral gain. In (18), the PI controller is used to increase the low frequency gain and ensure a good dynamic response of the system, while the resonant (R) controller is used to achieve zero steady-state error tracking of the grid current.

Referring to Fig. 2, the open-loop transfer function of the current loop with the proposed PIR controller is obtained as

$$G_{o-PIR}(s) = G_i(s)G_d(s)G_f(s)K_{pwm} \frac{1}{Ls+r} (1 + \Delta k_i) \quad (19)$$

To ensure fast dynamics, maintain good steady-state performance of the system, and eliminate the dc current injection caused by disturbances and the grid voltage measurement errors, the design requirements of the PIR controller are listed as follows:

- 1) A large phase margin (PM),  $PM \geq 45^\circ$ , is set to ensure a good dynamic response and robustness.
- 2) The gain at the low frequency band ( $\leq 1$  Hz) is larger than 50 dB to ensure good dc current injection suppression.
- 3)  $|G_{o-PIR}(j\omega_0)| \geq 50$  dB is set for small steady-state errors.

As the R controller only provides a large gain at the frequency close to the selected resonance frequency ( $\omega_0$ ), and the crossover frequency  $f_c$  of the system is usually set far away from  $\omega_0$ , the PIR controller can be approximated to be a PI controller at the low frequency band and the frequencies higher than  $f_c$  [32]. Thus, when the requirements 1) and 2) are considered, the PIR controller is simplified as

$$G_i(s) = k_p + \frac{k_i}{s} \quad (20)$$

According to (19), the PM of the system is expressed as

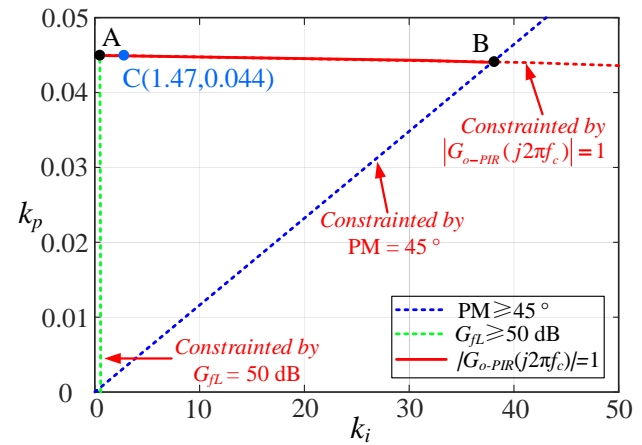


Fig.5. Regions of the control gain  $k_p$  and  $k_i$  constrained by the design requirements of 1) and 2).

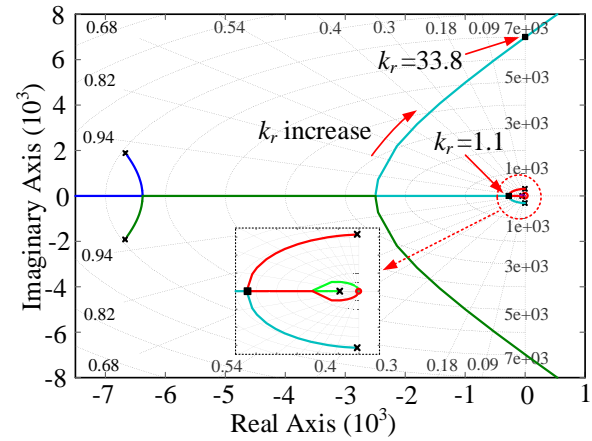


Fig.6. Root locus of the current loop with the gain  $k_r$ , varying from 0 to infinity.

$$PM = 180^\circ + \angle \frac{G_i(s)G_d(s)G_f(s)K_{pwm}(1 + \Delta k_i)}{Ls+r} \Big|_{s=j2\pi f_c} \quad (21)$$

To facilitate the analysis, the scaling error  $\Delta k_i$  in the grid current measurement is assumed as zero in the controller design. Then, substituting (20) into (21) gives

$$PM = 90^\circ + \arctan \frac{2\pi f_c k_p}{k_i} - \arctan 3\pi T_s f_c - \arctan 2\pi T_f f_c - \arctan \frac{2\pi f_c L}{r} \quad (22)$$

For  $|G_{o-PIR}(j2\pi f_c)| = 1$ , the relationship of  $k_p$  and  $k_i$  is obtained as

$$4\pi^2 f_c^2 k_p^2 + k_i^2 = \frac{4\pi^2 f_c^2 (4\pi^2 f_c^2 L^2 + r^2) (9\pi^2 f_c^2 T_s^2 + 1) (4\pi^2 f_c^2 T_f^2 + 1)}{K_{pwm}^2} \quad (23)$$

The gain at low frequency  $f_L$  is then expressed as

$$G_{fL} = 20 \log_{10} |G_{o-PIR}(j2\pi f_L)| = 20 \log_{10} \left( \frac{K_{pwm} \sqrt{4\pi^2 f_L^2 k_p^2 + k_i^2}}{2\pi f_L \sqrt{(4\pi^2 f_L^2 L^2 + r^2) (9\pi^2 f_L^2 T_s^2 + 1) (4\pi^2 f_L^2 T_f^2 + 1)}} \right) \quad (24)$$

Based on the design requirements of 1) and 2), the satisfactory region of  $k_p$  and  $k_i$  can be obtained once  $f_c$  and  $f_L$  are determined. Generally,  $f_c$  can be set as one tenth of the sampling frequency to ensure fast dynamics. However, owing to the

$$k_r = \sqrt{10^{\frac{G_{f_0}}{20}} \frac{(4\pi^2 f_0^2 L^2 + r^2)(9\pi^2 f_0^2 T_s^2 + 1)(4\pi^2 f_0^2 T_f^2 + 1)}{K_{pwm}^2} - \frac{k_i^2}{4\pi^2 f_0^2} - k_p} \quad (26)$$

$$G_{o-k_r}(s) = \frac{2k_r K_{pwm} \omega_c s^2}{(s^2 + 2\omega_c s + \omega_0^2) \{1.5LT_s T_f s^3 + (1.5rT_s T_f + 1.5LT_s + LT_f) s^2 + (1.5rT_s + rT_f + k_p K_{pwm} + L) s + r + k_i K_{pwm}\}} \quad (27)$$

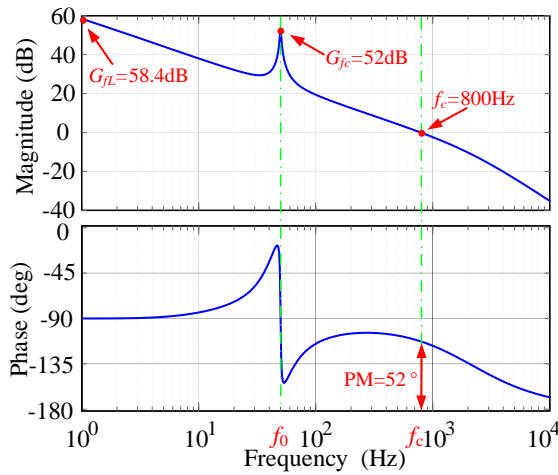


Fig.7. Bode diagram of  $G_{o-PIR}(s)$  with the designed controller.

control delay and sampling delay in practice, the large current loop bandwidth will cause stability issue. With this, in this study,  $f_c$  is set as approximately 4% of the sampling frequency  $f_s$  (i.e., 0.8 kHz) to achieve a sufficient PM and small overshoot [33]. Considering the dc offset of the grid voltage measurement and disturbances vary at a low frequency, it is reasonable to set  $f_L$  as 1 Hz to ensure an enough gain. According to the system parameters in Table I, the satisfactory region of  $k_p$  and  $k_i$  is depicted, as shown in Fig. 5. The red solid line from point A to B includes all the possible  $k_p$  and  $k_i$  that meet the aforementioned design requirements. To reduce the order of the system, the pole-zero compensation technique is used. Thus, the controller gains  $k_p$  and  $k_i$  are selected as  $k_p/k_i=L/r$ . Consequently, the point C shown in Fig.5 is a proper design. However, it should be noted that as the R controller can introduce negative phase shift at the frequencies higher than the resonant frequency, the PM will not hold. Therefore, it is necessary to check the system PM. If it does not meet the design requirements, the crossover frequency  $f_c$  should be adjusted following a few iterations of  $k_p$  and  $k_i$ .

Regarding the design of the R controller,  $\omega_c$  is the cut-off frequency. In view of a typical  $\pm 1\%$  variation of the grid fundamental frequency [34], the  $\omega_c$  is set as  $1\% \cdot 2\pi f_0 = \pi$  rad/s. To satisfy the requirement 3), the gain at resonant frequency  $f_0$  should be calculated first, it is shown as

$$\begin{aligned} G_{f_0} &= 20 \log_{10} |G_{o-PIR}(s)|_{s=j2\pi f_0} \\ &= 20 \log_{10} \left| \frac{G_i(s)G_d(s)G_f(s)K_{pwm}}{Ls + r} \right|_{s=j2\pi f_0} \end{aligned} \quad (25)$$

where  $G_i(s)$  is the PIR controller.

Rewriting (25), the resonant gain  $k_r$  is expressed as (26), shown at the top of this page. From (26), it can be seen that increasing  $k_r$  contribute to increase the gain at the frequency  $f_0$ . Thus, to meet the requirement 3), it is better to select  $k_r$  as large as possible. However, it will degrade the system stability, which limits the range of the gain  $k_r$ . According to (19), the equivalent open-loop transfer function related to the gain  $k_r$  is given in (27). Thus, the root locus of the current loop with  $k_r$  varying from 0 to infinity is depicted in Fig.6, where the

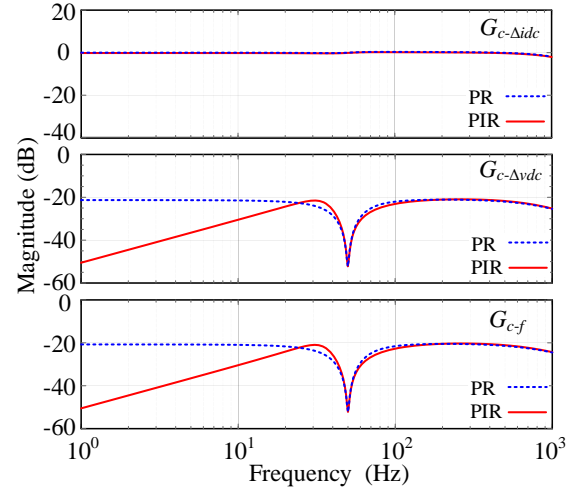


Fig.8. Bode diagram of  $G_{c-Dc}(s)$ ,  $G_{c-Dvdc}(s)$  and  $G_{c-f}(s)$  with a PR or a PIR controller.

system parameters are listed in Table I. From Fig.6, it can be seen that the closed-loop system is stable when  $k_r < 33.8$ . To achieve a sufficient stability margin as well as meet the requirement  $G_{f_0} \geq 50$  dB,  $k_r$  is set as 1.18 in this paper, where two dominant poles are located at the same place in the real axis. Fig.7 then shows the Bode diagram of the open-loop transfer function  $G_{o-PIR}(s)$  with the designed controller parameters. As it can be observed in Fig.7, the crossover frequency  $f_c$  of the system is 800 Hz with the PM being  $52^\circ$  and the gain at fundamental frequency  $f_0$  being 52 dB. This indicates that the system is stable with a good steady-state and dynamic performance.

### B. Evaluation of the DC Current Suppression Capability

Substituting the proposed PIR controller into (5), (7) and (8), the magnitude of  $G_{c-Dc}(s)$ ,  $G_{c-Dvdc}(s)$  and  $G_{c-f}(s)$  at the low frequency  $f_L$  determines the magnitude of the injected dc current. From (5), (7) and (8), we have

$$G_{c-Dc} = 20 \log_{10} \left| \frac{i_g(s)}{\Delta i_{dc}(s)} \right|_{s=j2\pi f_L} \quad (28)$$

$$G_{c-Dvdc} = 20 \log_{10} \left| \frac{i_g(s)}{\Delta v_{dc}(s)} \right|_{s=j2\pi f_L} \quad (29)$$

$$G_{c-f} = 20 \log_{10} \left| \frac{i_g(s)}{f(s)} \right|_{s=j2\pi f_L} \quad (30)$$

Thus, the dc current caused by grid current and voltage measurement errors and disturbances is determined as

$$I_{dc-Dc} = \Delta i_{dc} 10^{\frac{G_{c-Dc}}{20}} \quad (31)$$

$$I_{dc-Dvdc} = \Delta v_{dc} 10^{\frac{G_{c-Dvdc}}{20}} \quad (32)$$

$$I_{dc-f} = f 10^{\frac{G_{c-f}}{20}} \quad (33)$$

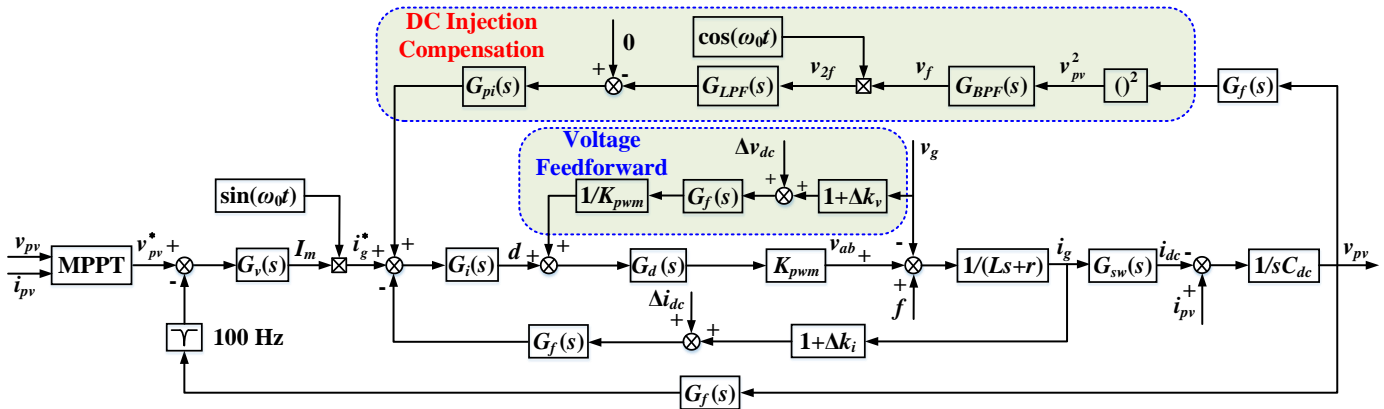


Fig. 9. Block diagram of the entire control scheme of the single-phase inverter with the proposed control and compensation scheme.

Fig. 8 shows the frequency response of  $G_{c-\Delta idc}(s)$ ,  $G_{c-\Delta vdc}(s)$  and  $G_{c-f}(s)$ , where PR controller and PIR controller are adopted in the current loop. In Fig. 8, the magnitude of  $G_{c-\Delta vdc}(s)$  at the low frequency  $f_L$  (1Hz) with the PR and PIR controller are 20.6 and 50.4 dB, respectively. By contrast, the magnitude of  $G_{c-f}(s)$  at the low frequency  $f_L$  with the PR and PIR controller are 20.3 and 50.2 dB, respectively. Thus, according to (32) and (33), the injected dc current caused by the grid voltage measurement error can be approximately determined as  $I_{dc-\Delta vdc}=0.093\Delta vdc$  with the PR controller and  $I_{dc-\Delta vdc}=0.003\Delta vdc$  with the proposed PIR controller. Similar results can be obtained from  $G_{c-f}(s)$  with the PR and PIR controller. Obviously, due to the large low frequency gain of the proposed controller, the injected dc current caused by the grid voltage measurement error and disturbances can be mitigated to a large extent. Nevertheless, as shown in Fig.8, the magnitude of  $G_{c-\Delta idc}(s)$  at the low frequency  $f_L$  with the PR and PIR controller is nearly 0 dB, which indicates that the injected dc current induced by the grid current measurement errors cannot be mitigated by the current controller.

#### IV. PROPOSED DC INJECTION COMPENSATION SCHEME

From the above, it is known that the current controller cannot suppress the dc component resulted from the grid current measurement errors. This is because the grid current is the feedback signal of the current controller, utilizing the current controller to suppress the dc injection caused by measurement errors in the feedback path will be ineffective. Thanks to the physical relationship between the dc current injection and the line-frequency ripple of the dc-link voltage, as shown in Section II-C, the dc component produced by grid current measurement error can be estimated indirectly. As a result, an effective dc injection compensation scheme is developed.

##### A. Proposed DC Injection Compensation Scheme

From (17), the dc-link line-frequency voltage ripple caused by the dc injection of the grid current is derived as

$$\begin{aligned} \frac{dv_f}{dt} &= -\frac{2I_{DC}V_m}{C_{dc}} \sin(\omega_0 t) \\ \Leftrightarrow v_f &= \frac{2I_{DC}V_m}{C_{dc}\omega_0} \cos(\omega_0 t) \end{aligned} \quad (34)$$

where  $v_f$  is the line-frequency ripple of the dc-link voltage  $v_{pv}^2$ .

In order to extract the line-frequency ripple  $v_f$  from  $v_{pv}^2$ , a band-pass filter with the central frequency at  $\omega_0$  is introduced as

$$G_{BPF}(s) = \frac{\omega_b s}{s^2 + \omega_b s + \omega_0^2} \quad (35)$$

where  $\omega_b = 2\pi$  (rad/s) is the bandwidth of the band-pass filter.

The obtained line-frequency voltage ripple  $v_f$  is then multiplied by  $\cos(\omega_0 t)$ , and thus, a dc component proportional to  $I_{DC}$  is generated, which is expressed as

$$v_{2f} = \frac{I_{DC}V_m}{C_{dc}\omega_0} + \frac{I_{DC}V_m}{C_{dc}\omega_0} \cos(2\omega_0 t) \quad (36)$$

Following, a second-order low-pass filter (LPF) shown in (37) is then used to extract the dc component.

$$G_{LPF}(s) = \frac{\omega_n^2}{s^2 + \xi\omega_n s + \omega_n^2} \quad (37)$$

where  $\xi$  is the damping coefficient and  $\omega_n$  is the natural angular frequency. They are set as 1 and  $20\pi$  (rad/s), respectively.

Subsequently, the estimated dc component is expressed as

$$v_{dc} = \text{LPF}\{v_{2f}\} = \frac{I_{DC}V_m}{C_{dc}\omega_0} \quad (38)$$

After the dc component is estimated by (38), it can be eliminated through an indirect compensation loop. Fig. 9 shows the entire control and compensation block diagram of the single-phase inverter system, where  $G_{sw}(s)$  represents the switching function of the inverter, and  $G_{pi}(s)$  is a PI controller that is utilized to suppress the dc injection by controlling the estimated dc component to zero. Notably, as it can be seen in Fig. 9, since the dc-link voltage reference generated by MPPT algorithm changes very slowly, it can be viewed as a constant. Therefore, if the bandwidth of voltage loop is high, the dc-link voltage can track it reference well, which will lead to the dc-link voltage ripple to be significantly attenuated and the grid current to be greatly distorted. So, in this study, the voltage loop bandwidth is set 20 Hz. This low bandwidth is helpful for blocking the line-frequency ripple from penetrating into the current loop. And thus, it is beneficial for the proposed compensation strategy.

##### B. Evaluation of the DC Injection Rejection Capability

To evaluate the proposed compensation scheme, the equivalent control block diagram of the dc injection



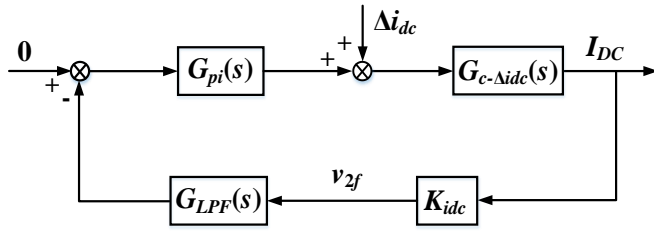


Fig.10. Equivalent control block diagram of the proposed compensation scheme.

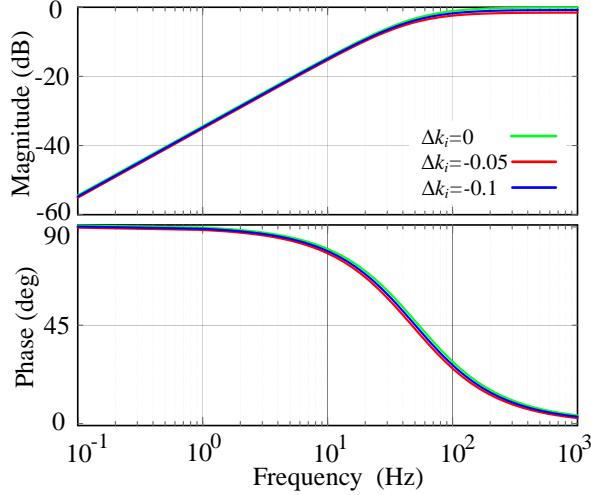


Fig. 11. Bode diagram of transfer function  $G_{c-\Delta i_{dc}}(s)$  with the proposed dc injection compensation scheme.

suppression is shown in Fig. 10, where  $K_{idc}$  is the steady-state gain from the dc injection  $I_{DC}$  to  $v_{2f}$ , it is shown as

$$K_{idc} = \frac{V_m}{2C_{dc}\omega_0} \quad (39)$$

The detailed derivation of  $K_{idc}$  can be found in the Appendix II. Since we only focus on the very low frequency range,  $G_{c-\Delta i_{dc}}(s)$  and  $G_{LPF}(s)$  can be approximated as gains, shown as

$$G_{c-\Delta i_{dc}}(s) = \frac{G_i(s)G_d(s)G_f(s)K_{pwm}}{Ls + r + G_i(s)G_d(s)G_f(s)K_{pwm}(1 + \Delta k_i)} \Big|_{s=j2\pi \cdot 0} \approx \frac{1}{1 + \Delta k_i} \quad (40)$$

$$G_{LPF}(s) = \frac{\omega_n^2}{s^2 + \zeta\omega_n s + \omega_n^2} \Big|_{s=j2\pi \cdot 0} \approx 1 \quad (41)$$

Thus, the closed-loop transfer function of the system from  $\Delta i_{dc}$  to  $I_{DC}$  is obtained as

$$G_{c-\Delta i_{dc}}(s) = \frac{I_{DC}}{\Delta i_{dc}} = \frac{1/(1 + \Delta k_i)}{1 + \frac{1}{1 + \Delta k_i} \frac{V_m}{2C_{dc}\omega_0} (k_{pdc} + \frac{k_{idc}}{s})} \quad (42)$$

Regarding the parameters selection of the PI controller, the rule is to ensure the closed-loop transfer function  $G_{c-\Delta i_{dc}}(s)$  has a large attenuation gain at the low frequency range. In this paper, the proportional gain  $k_{pdc}$  and integral gain  $k_{idc}$  are set as 0.0003 and 1, respectively. Fig. 11 shows the Bode diagram of the closed-loop transfer function  $G_{c-\Delta i_{dc}}(s)$  with the scaling error  $\Delta k_i$  of the grid current measurement varying from -0.1 to 0. As it can be observed in Fig. 11, the gain at the low frequency  $f_L$  (1Hz) is -33 dB. Thus, the injected dc current can be suppressed to a large extent. What's more, even if the scaling error in the grid current measurement is around -0.1, the

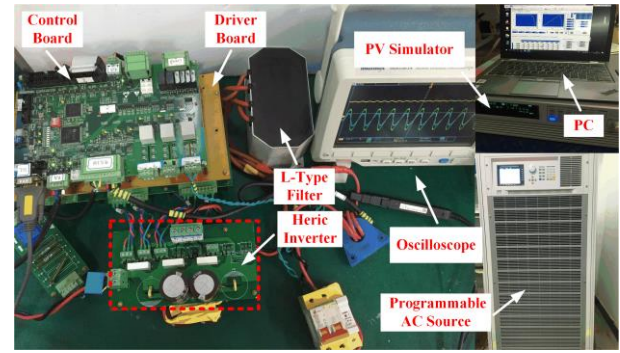


Fig.12. Experimental setup of the 1.2-kW single-phase HERIC inverter system.

TABLE I  
EXPERIMENTAL PARAMETERS

Parameters	Values	Parameters	Values
Output Power: $P_o$	1.2 kW	Filter delay time: $T_f$	39.6 $\mu$ s
MPP voltage: $v_{pv}$	220 V	Proportional gain: $k_p$	0.042
Grid voltage: $v_g$ (rms)	110 V	Integral gain: $k_i$	1.4
Grid frequency: $f_g$	50 Hz	Resonant gain: $k_r$	1.18
Switching frequency: $f_{sw}$	20 kHz	Cutoff frequency: $\omega_c$	$\pi$
Sampling frequency: $f_s$	20 kHz	Proportional gain: $k_{pdc}$	0.0003
Filter inductor: $L$	3 mH	Integral gain: $k_{idc}$	1
Equivalent resistance: $r$	0.1 $\Omega$	DC-link capacitor: $C_{dc}$	1400 $\mu$ F

TABLE II  
THE VALUES OF DC INJECTION SOURCE

Parameters	Values	Parameters	Values
Disturbance: $f$	2 V	Scaling error in current measurement: $\Delta k_i$	-0.03
DC offset in voltage measurement: $\Delta v_{dc}$	4 V	DC offset in current measurement: $\Delta i_{dc}$	0.2 A
Scaling error in voltage measurement: $\Delta k_v$	-0.03		

TABLE III  
CONDITIONS OF THE EXPERIMENTAL TESTS

Cases	$f$	$\Delta v_{dc}$	$\Delta k_i$	$\Delta i_{dc}$	$\Delta k_v$	DC injection suppression strategy	Solar irradiance step change
Case I	✓	✓	✗	✓	✗	PR	✗
Case II	✓	✓	✓	✓	✗	PR	✗
Case III	✓	✓	✗	✓	✗	PIR	✗
Case IV	✓	✓	✓	✓	✗	PIR + Compensation	✗
Case V	✓	✓	✓	✓	✗	PR + Virtual capacitor	✗
Case VI	✓	✓	✓	✓	✗	PIR + Compensation	✓
Case VII	✓	✗	✓	✗	✗	PIR	✗

impact on the low frequency attenuation is negligible. In all, the proposed compensation strategy has strong ability to reject the dc current injection.

## V. EXPERIMENTAL RESULTS

A 1.2-kW single-phase transformerless grid-connected PV inverter prototype, as shown in Fig. 12, has been built and tested to verify the effectiveness of the proposed method. The controller is implemented by a floating-point digital signal processor (DSP) TSM320F28335 and the gate-driving signals of the IGBT devices are generated by a field programmable gate array (FPGA) EP2K8T144C8N. A HIOKI 3390 power analyzer is used to measure the power quality of the grid voltage and current. A Chroma PV simulator and a programmable ac source are adopted to imitate the PV array and the power grid, respectively. The key experimental parameters are listed in Table I.

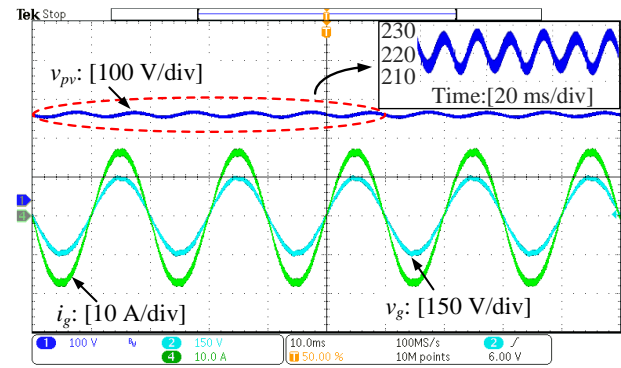
Notably, as the dc-link line-frequency voltage ripple is utilized in the proposed dc injection compensation scheme and its value is small, the sampling precision of the conditioning circuit for the dc-link voltage should be considered. Therefore, two improvements were made in the dc-link voltage conditioning circuit: 1) The precision of the sampling resistor and operational amplifier in the conditioning circuit is improved; 2) In the conditioning circuits, a fixed constant voltage value, e.g., 180V (3V in the conditioning circuit), which is slightly higher than the amplitude of the grid voltage, is subtracted from the measured dc-link voltage. Then, the actual voltage is restored in the DSP by adding the subtracted voltage, i.e., 180V. Based on the above two improvements, the sampling precision of the dc-link voltage meets the requirements in practice. It is worth noting that the dc-link voltage sampling is realized by a resistance voltage divider. Thus, although the accuracy of sampling resistance is improved, it is still economical when compared with active hardware strategies. To verify the effectiveness of the proposed method, the following seven cases are considered, where the values of the disturbance, scaling error and dc offset in the voltage and current measurement are taken from practical applications, as shown in Table II. All the testing conditions are summarized in Table III and described in the following:

1) *Case I*: The grid voltage and current have dc offsets as given in Table II, while the scaling error is zero. There are disturbances in the system. A typical PR controller is adopted in the current loop according to the discussions in previous sections.

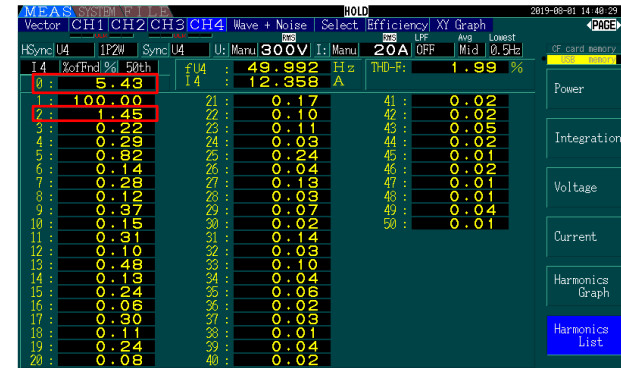
2) *Case II*: The grid voltage and current have dc offsets, the scaling error of the current measurement is -0.03. There are disturbances in the system. The PR controller is adopted in the current loop like *Case I*. This study case is used to verify the impact of the current scaling error measurement on the dc current injection in the system.

3) *Case III*: The grid voltage and current have dc offsets, while the scaling error is zero. Disturbances also appear in the system. The proposed PIR controller is then adopted in the current loop. This case is designed to evaluate the capability of the PIR controller to suppress the dc component caused by the grid voltage dc offset measurement and disturbances.

4) *Case IV*: The grid voltage and current have dc offsets, the scaling error of the current measurement is -0.03. Disturbances are also considered in this case. The proposed PIR control and dc injection compensation scheme is activated in order to



(a)



(b)

Fig. 13. Experimental results of the inverter with the PR controller under disturbances and dc offset. (a) Experimental waveform, (b) the fast Fourier transform (FFT) analysis of the grid current.

verify the effectiveness of the proposed dc injection suppression method for single-phase inverters.

5) *Case V*: The grid voltage and current have dc offsets, the scaling error of current measurement is -0.03. The disturbances are also present in the system. The virtual capacitor method in [13] is adopted in order to compare the performance of the proposed method.

6) *Case VI*: The grid voltage and current have dc offsets, while in this case, the scaling error of the current measurement is -0.03. There are disturbances in the system. The proposed PIR control and dc injection compensation scheme is activated. The solar irradiance step changes from 1000 W/m<sup>2</sup> to 500 W/m<sup>2</sup> to demonstrate the dynamics and robustness of the system.

7) *Case VII*: The grid voltage and current measurement do not contain dc offsets. The disturbances caused by the disparity of power modules and asymmetry of driving pulses always appear in the system. In this case, only the current loop is adopted in the system (the input of inverter is connected with a dc voltage source) and the scaling error of the current measurement is set as 0.1 to clearly show its impact on the grid current reference tracking and grid voltage disturbance suppression. The proposed PIR control is activated in the current loop.

### A. Case I

To clearly show the dc injection issue in the transformerless PV inverter system, all possible sources, i.e., the disturbances, the dc offset in the grid voltage and current measurement, are considered in this case. Fig. 13 shows the experimental results

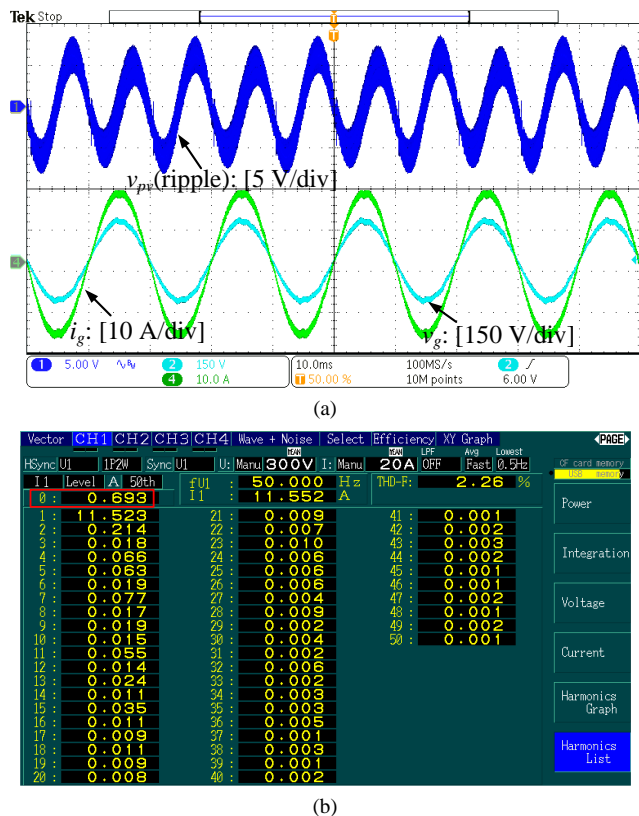


Fig. 14. Experimental results of the inverter with the PR controller in the case that the system contains disturbance, grid voltage measurement dc offsets, current measurement dc offset and scaling errors. (a) Experimental waveform; (b) Harmonic level.

of the inverter system with a traditional PR controller in the current loop. From Fig. 13, it can be seen that the dc component in the grid current is 5.43%, which is far higher than 0.5% required in the IEEE Standard 1547-2018 [7]. Furthermore, as analyzed in Section II, the dc component injected into grid will lead to the line-frequency ripple in the dc-link voltage, which increases the 2nd-order harmonics of the grid current. As shown in Fig. 13(a) and (b), the ripple of the dc-link voltage contains line-frequency component and the 2nd-order harmonics of the grid current exceed the threshold in the standards [7]. In all, the results verified the theoretical analysis presented in Section II.

### B. Case II

To verify the impact of the grid current measurement scaling error on the dc injection of system, the scaling error in the grid current measurement is set as -0.03. In this test, the disturbances, dc offset in the grid voltage and current measurement are given in Table II. The same experiment test as Case I is considered and the results are shown in Fig. 14. As shown in Fig. 14, since the negative scaling error in the grid current measurement can increase the dc component caused by the dc offset in the current measurement, the dc component of the grid current is higher than that shown in Fig. 13, which goes up to 5.61%, as compared in Table IV. As a result, the higher dc component increases the line-frequency ripple in the dc-link voltage and then further deteriorates the power quality of the grid current. This results in a total harmonic distortion (THD) of the grid current being 2.26%, which was 1.98% in

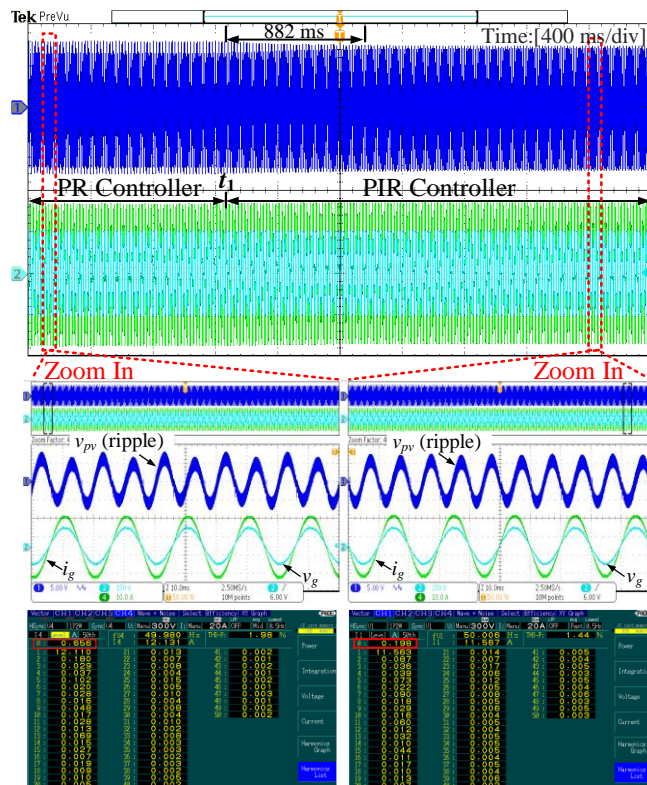


Fig. 15. Experimental results of the inverter with the PIR controller in the case that the system contains disturbances, dc offsets in the grid voltage and current measurement.

TABLE IV  
THD AND DC CURRENT COMPONENT OF THE GRID CURRENT

Test Case	DC Component	2nd-order Harmonic (%)	THD (%)
I	5.43% (0.656A)	1.45	1.98
II	5.61% (0.693A)	1.66	2.26
III	1.68% (0.198A)	0.53	1.44
IV	0.24% (0.022A)	0.29	1.25
V	1.72% (0.204A)	0.55	1.45
VI	0.27% (0.025A)	0.32	1.36

Case I. In all, the experimental results are consistent with the theoretical analysis.

### C. Case III

To demonstrate the effect of the PIR controller on the dc component suppression, the experiment of the inverter with the grid current controller being the proposed PIR controller under the same conditions of Case I is performed. The results are shown in Fig. 15. As it can be observed in Fig. 15, when the integral term is added into the controller at  $t_1$ , the grid current is effectively regulated to be sinusoidal and the dc component is reduced from 5.43% to 1.68%, as compared in Table IV. Thus, it can be concluded that the integral controller added into the current loop contributes the suppression of the dc component of the grid current to a large extent. Nevertheless, the dc component in the grid current is 1.68% (about 0.2 A), which still exceeds the IEEE Standard 1547-2018. This is because, as analyzed in section II-B, the dc

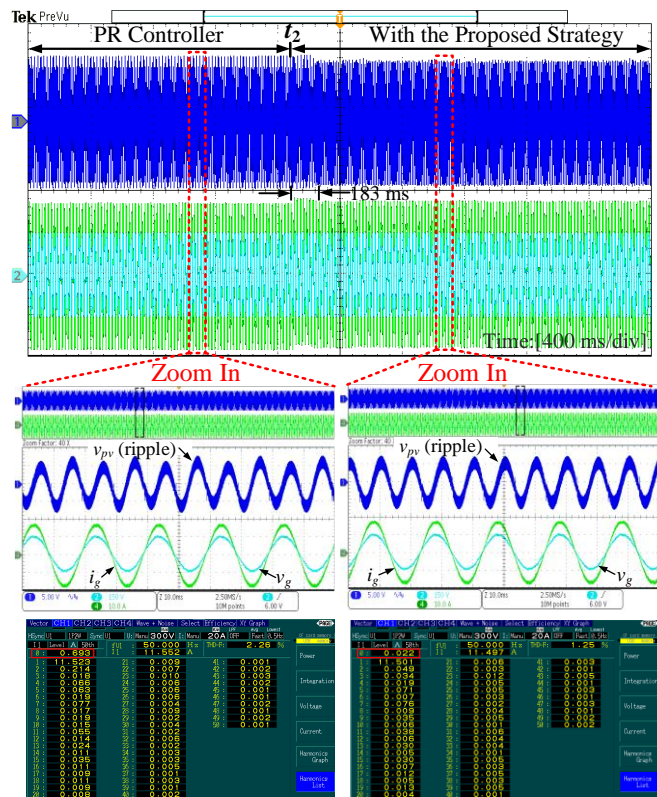


Fig. 16. Experimental results of the inverter with the proposed dc injection compensation strategy in the case that the system contains disturbances, dc offsets in the voltage measurement and dc offset and scaling errors in the current measurement.

component caused by the dc offset in the grid current measurement cannot be eliminated only by the closed-loop current controller. Therefore, in order to further suppress the dc component, a more effective solution should be developed.

#### D. Case IV

To verify the efficacy of the proposed compensation method, further experimental tests are carried out. The results are shown in Fig. 16. This case is similar to Case II, where the current controller is the PR controller before  $t_2$ , and the system has disturbances, dc offset and scaling error in the voltage and current measurement. Observations from Fig.16 imply that, when the integral term and the compensation strategy are activated at  $t_2$ , the dc component in the grid current is mitigated from 5.61% to 0.24% (see Table IV) with less than 0.2s. However, it is worth noting that, as shown in Section IV-B, the theoretical gain of the proposed compensation loop at the low frequency  $f_L$  (1Hz) is -33 dB, which means that the dc component caused by the dc offset in the grid current measurement can be mitigated to be nearly zero. The reason for this discrepancy is that the precision of the dc-link voltage sampling is limited in practice. When the dc component of the grid current is reduced to a small value, the dc-link voltage line-frequency ripple will be also very small, which increases the difficulty of the ripple measurement. Nevertheless, the results completely comply with the IEEE 1547-2018 dc current injection limit standards, i.e., <0.5%. In addition, after the proposed method is activated, the ripple in the dc-link voltage purely varies at the double-line frequency. Thus, it benefits to the reduction of the 2nd-order harmonic component of the grid current. In this case, the 2nd-order harmonic and the

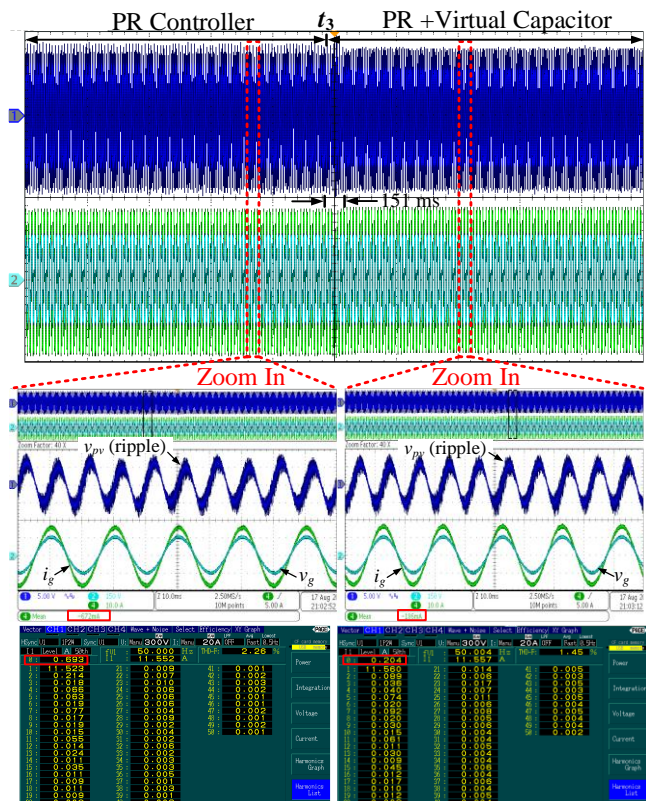


Fig.17. Experimental results of the inverter with the virtual capacitor strategy in the case that the system contains disturbance, grid voltage measurement dc offsets, current measurement dc offsets and scaling errors.

THD of the grid current is 0.29% and 1.25%, respectively, as shown in Table IV, achieving a good power quality. From the above tests, it has been verified that the proposed method is of cost-effectiveness for the dc injection suppression.

#### E. Case V

To further demonstrate the superior performance of the proposed method, an active software dc suppression solution called the virtual capacitor method [13] is tested to make a comparison. To avoid large voltage drops, the capacitance of the virtual capacitor is set as 2000  $\mu\text{F}$ . Fig. 17 shows the experimental results of the grid current and the dc-link voltage with the virtual capacitor method under the same conditions of Case IV. As presented in Fig. 17, when the virtual capacitor strategy is activated at time  $t_3$ , the dc component of the grid current is reduced from 5.61% to 1.72% (see Table IV) with the dynamic time being 0.15 s. Although the dc component is reduced rapidly and significantly, it is still beyond the limitation, i.e., 0.5% in the IEEE Standard 1547-2018. Moreover, the dc component is 0.204 A (see Table IV) after the virtual capacitor strategy is activated, which is equal to the dc bias caused by the current measurement. In all, the experimental results have verified the analysis in Section I, since the dc bias induced by current sensors and sampling circuits is in the controller feedback channel, it is difficult to eliminate it by a current feedback control. As it has been quantitatively summarized in Table IV, with the proposed method, not only the injected dc current is significantly reduced but also the power quality of the grid current is increased. Hence, the proposed method can be a cost-effective solution to the dc current injection for single-phase inverters.

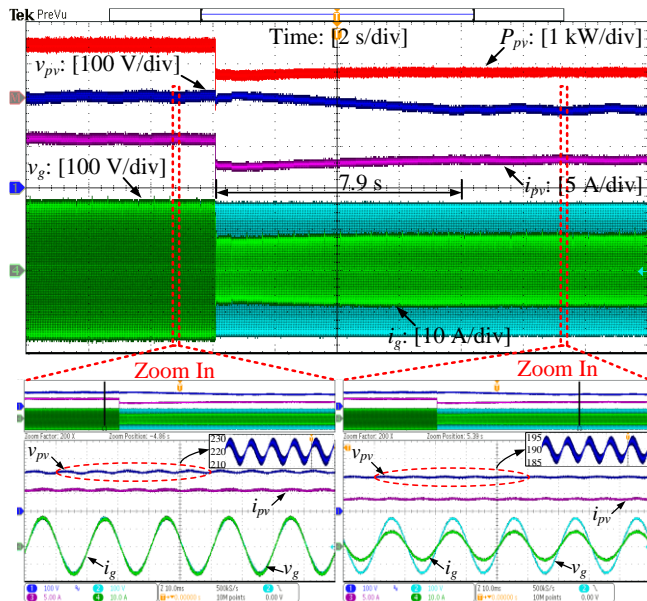


Fig. 18. Experimental results of the system with the proposed dc current injection suppression strategy in the case that the irradiance is suddenly changed from 1000 W/m<sup>2</sup> to 500 W/m<sup>2</sup>.

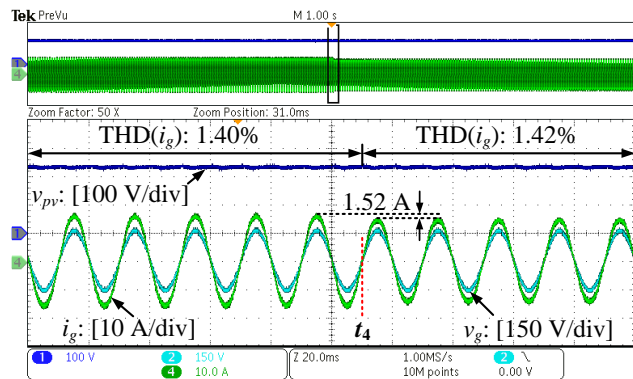


Fig. 19. Experimental results of the inverter in the case that the scaling error of the grid current measurement  $\Delta k_i$  is suddenly changed from 0 to 0.1.

#### F. Case VI

To show the dynamics and robustness of the system with the proposed dc current injection suppression strategy, the experiment in the case of solar irradiance step change from 1000 W/m<sup>2</sup> to 500 W/m<sup>2</sup> was tested. In this case, a perturb and observe (P&O) MPPT algorithm is employed with the updating time is 0.5 s and the step size is 4 V. Fig. 18 shows the experimental results. As it is observed in Fig. 18, despite the step change of irradiance, the system is still stable with the MPPT time is 7.9 s. In addition, when the irradiance changed from 1000 W/m<sup>2</sup> to 500 W/m<sup>2</sup>, the dc component of grid current is slightly increased from 0.24% to 0.27% (see Table IV Case IV and VI), nevertheless, it is still below the standard limit (i.e., 0.5%). From this result, it can be concluded that the proposed dc current injection suppression strategy is effective and suitable for PV generation system.

#### G. Case VII

To show the impact of scaling error in grid current measurement on the grid current reference tracking and grid voltage disturbance suppression, the scaling error is set as 0.1 and only the current loop is adopted (the input of inverter is connected with a dc voltage source) in this case. Fig. 19 shows

the experimental results of the inverter system, where the scaling error in grid current measurement  $\Delta k_i$  is suddenly changed from 0 to 0.1 at  $t_4$ . It can be observed that, although the scaling error of grid current is 0.1, the inverter system achieves a sinusoidal grid current and the THD of current is almost the same. However, after the step change in  $\Delta k_i$ , there exists a considerable steady-state error in grid current (approximately 1.52A). This is because, as analyzed in Section II-B, the scaling error in grid current measurement will lead to current tracking errors. Consequently, this result verified the correctness of theoretical analysis.

TABLE V

COMPARISONS OF THE PROPOSED METHOD WITH THE PRIOR-ART SCHEMES

Method (year)	Steady-state DC Component ( mA)	Transient time (s)	Cost
[21] (2018)	2 mA	–	High
[19] (2018)	5 mA	60 s	Medium
[27] (2018)	30 mA	3 s	Low
[25] (2019)	109 mA, 31 mA and 78 mA (phase a, b, c)	0.03 s	Low
Proposed	22 mA	0.18 s	Low

#### H. Comparisons with Existing Solutions

To further show the performance of the proposed dc current suppression strategy, a detailed comparison is carried out among the proposed method and the prior-art dc component suppression schemes in terms of steady-state, dynamic performance and cost. The results are shown in Table V. As it can be observed in Table V, although the coupled inductor-based technique [21] achieved the lowest dc component, it is costly, since a coupled inductor combined with a high accuracy Hall effect current sensor were adopted to directly measure the dc component. To reduce the cost, alternative active hardware method was proposed in [19], where the dc component was detected by measuring the inverter output voltage and then mitigated through a compensation loop. Furthermore, according to Table V, although the method in [19] achieves a good steady-state performance, the dynamic performance is the worst. To further reduce the cost, the active software solutions were proposed in [25] and [27]. With the help of the neural network PID controller in the dc component compensation loop, the PID parameters can be adjusted adaptively and the shortest transient time is achieved in [25]. However, as aforementioned, since the dc component information is directly obtained from the grid current by using a sliding window double integration method, the dc bias caused in the current measurement cannot be eliminated by the current feedback control. The steady-state results shown in [25] confirmed this conclusion, where the dc component is 109 mA, 31 mA and 78 mA in phase a, b and c, respectively. The method in [27] achieves moderate steady-state and dynamic performance. Yet, it is also shown in Table V that the proposed strategy outperforms it both in steady-state and dynamic performance. As good dc current suppression performance and low cost are of importance in PV generation systems, the proposed method is very suitable for PV applications.

## VI. CONCLUSION

The dc current injection in grid-connected inverters lead to transformer saturation and current distortions. To address the issues, this paper explored the root-causes of the dc current injection and its impact on grid-connected PV inverters. The exploration shows that the dc component caused by the grid voltage measurement errors and disturbances can be eliminated by increasing the current controller gain at the low frequency. A PIR controller was then employed to achieve a high gain in the low frequency band. A step-by-step controller parameters design, including the loop-gain, phase margin and bandwidth, was presented to realize the dc injection suppression with high control performance. To eliminate the dc current induced by grid current measurement errors, which cannot be suppressed by the current controller, a simple compensation method was proposed. The injected dc current was estimated by extracting the line-frequency voltage ripple on the dc-link voltage, and then, it was reduced by adding a dc component control loop. The detailed design guidelines of the proposed compensation method were described, and its dc injection rejection capability was evaluated and demonstrated experimentally. The various experimental cases and comparisons have verified the analysis and the efficacy of the proposed method.

### APPENDIX I

According to [35], the simplified mode of PV modules is shown as

$$i_{pv} = I_{sc} [1 - C_1 (e^{\frac{v_{pv}}{C_2 V_{oc}}} - 1)] \quad (A.1)$$

where

$$C_1 = (1 - \frac{I_{mpp}}{I_{sc}}) e^{-\frac{V_{mpp}}{C_2 V_{oc}}}, \quad C_2 = (\frac{V_{mpp}}{V_{oc}} - 1) \ln [1 - \frac{I_{mpp}}{I_{sc}}]^{-1} \quad (A.2)$$

where  $i_{pv}$  and  $v_{pv}$  are the PV current and voltage, respectively.  $I_{sc}$  is short circuit current,  $V_{oc}$  is open circuit voltage,  $I_{mpp}$  and  $V_{mpp}$  are the current and voltage at the maximum power point (MPP), respectively. According to (A.1) and (A.2), the PV output power  $P_{pv}$  can be estimated as (A.3) under the standard test condition (i.e. 25 °C, 1000 W/m<sup>2</sup>).

$$P_{pv} = f(v_{pv}) = v_{pv} I_{sc} [1 - C_1 (e^{\frac{v_{pv}}{C_2 V_{oc}}} - 1)] \quad (A.3)$$

TABLE VI  
PARAMETERS OF PV CELLS AT THE STANDARD TEST CONDITIONS

Parameters	Values	Parameters	Values
Short circuit current: $I_{sc}$	6.14 A	MPP current: $I_{mpp}$	5.45 A
Open circuit voltage: $V_{oc}$	282 V	MPP voltage: $V_{mpp}$	220 V

Based on the PV parameters shown in Table V and by taking the Taylor series of (A.3) at the MPP, we have

$$P_{pv} = 1193 - 0.1674(v_{pv} - 220) - 0.1244(v_{pv} - 220)^2 - 0.0016(v_{pv} - 220)^3 + \dots R_n(v_{pv}) \quad (A.4)$$

where  $R_n(v_{pv})$  is the remainder.

According to (A.4) and (17), it can be seen that, if there is no dc component in grid current, the dc-link voltage will not

contain the line-frequency ripple, and then there will no line-frequency power oscillation in PV output power.

### APPENDIX II

To obtain the steady-state gain from the dc injection  $I_{DC}$  to  $v_{2f}$ , a generalized state-space averaging (GSSA) method [36] which considers the average of state variables and harmonics is adopted. If the time-domain periodic variable meets the condition  $\int_0^T |x(t)|^2 < \infty$ ,  $x(t)$  can then be transformed in the period  $(t-T, t)$  by

$$x(t) = \sum_{k=-\infty}^{\infty} \langle x \rangle_k(t) e^{jk\omega t} \quad (A.5)$$

where  $\omega = 2\pi/T$  is the fundamental angular frequency, and  $\langle x \rangle_k(t)$  are the  $k$ -th Fourier coefficients that are defined by

$$\langle x \rangle_k(t) = \frac{1}{T} \int_{t-T}^t x(\tau) e^{-jk\omega \tau} d\tau \quad (A.6)$$

Eq. (A.5) and (A.6) lead to two fundamental properties of the GSSA, which is expressed as

$$\left\langle \frac{d}{dt} x \right\rangle_k(t) = \frac{d}{dt} \langle x \rangle_k(t) + jk\omega \langle x \rangle_k(t) \quad (A.7)$$

$$\langle xy \rangle_k = \sum_{i=-\infty}^{\infty} \langle x \rangle_{k-i} \langle y \rangle_i \quad (A.8)$$

According to (14), since only the fundamental frequency of ac variables is of interest, the generalized state-space averaging model is expressed as

$$\left\langle \frac{1}{2} C_{dc} \frac{dv_{pv}^2}{dt} \right\rangle_1 = \frac{1}{2} C_{dc} \left( \frac{d \langle v_{pv}^2 \rangle_1}{dt} + j\omega_0 \langle v_{pv}^2 \rangle_1 \right) = \langle v_{pv} i_{pv} \rangle_1 - \langle v_g i_g \rangle_1 \quad (A.9)$$

where

$$\frac{d \langle v_{pv}^2 \rangle_1}{dt} = 0; \quad \langle v_{pv} i_{pv} \rangle_1 = 0; \quad (A.10)$$

$$\langle v_g i_g \rangle_1 = \langle v_g \rangle_0 \langle i_g \rangle_1 + \langle v_g \rangle_1 \langle i_g \rangle_0 = -j \frac{V_m}{2} \langle i_g \rangle_0$$

Thus, the steady-state gain from  $I_{DC}$  to  $v_{pv}^2$  is derived as

$$\frac{\langle v_{pv}^2 \rangle_1}{\langle i_g \rangle_0} = \frac{V_m}{C_{dc} \omega_0} \quad (A.11)$$

Similarly, the steady-state gain from  $v_{pv}^2$  to  $v_f$ , shown in Fig. 9, can be derived as

$$\langle v_f \rangle_1 = G_{BPF}(j\omega_0) \langle v_{pv}^2 \rangle_1 = \langle v_{pv}^2 \rangle_1 \quad (A.12)$$

From  $v_f$  to  $v_{2f}$ , we only focus on the steady-state gain from the fundamental frequency to dc component, thus, we have:

$$\begin{aligned} \langle v_{2f} \rangle_0 &= \langle v_f \cos(\omega_0 t) \rangle_0 \\ &= \langle v_f \rangle_0 \langle \cos(\omega_0 t) \rangle_0 + \langle v_f \rangle_1 \langle \cos(\omega_0 t) \rangle_{-1} = \frac{1}{2} \langle v_f \rangle_1 \end{aligned} \quad (A.13)$$

Consequently, according to (A.11)-(A.13), the steady-state gain from  $\langle i_g \rangle_0$  i.e.  $I_{DC}$ , to  $\langle v_{2f} \rangle_0$  is derived as

$$\frac{\langle v_{2f} \rangle_0}{\langle i_g \rangle_0} = \frac{V_m}{2C_{dc} \omega_0} \quad (A.14)$$

## REFERENCES

- [1] T. Kerekes, R. Teodorescu, P. Rodriguez, G. Vazquez and E. Aldabas, "A new high-efficiency single-phase transformerless PV inverter topology," *IEEE Trans. Ind. Electron.*, vol. 58, no. 1, pp. 184-191, Jan. 2011.
- [2] B. Guo, M. Su, Y. Sun, H. Wang, B. Liu, X. Zhang, J. Pou, Y. Yang and P. Davari, "Optimization design and control of single-stage single-phase PV inverters for MPPT improvement," *IEEE Trans. Power Electron.*, vol. 35, no. 12, pp. 13000-13016, Dec. 2020.
- [3] M. N. H. Khan, M. Forouzesh, Y. P. Siwakoti, L. Li, T. Kerekes and F. Blaabjerg, "Transformerless inverter topologies for single-phase photovoltaic systems: a comparative review," *IEEE J. Emerg. Sel. Topics Power Electron.* Early Access. 2019.
- [4] K. Alluhaybi, I. Batarseh, H. Hu and X. Chen, "Comprehensive review and comparison of single-phase grid-tied photovoltaic microinverters," *IEEE J. Emerg. Sel. Topics Power Electron.* Early Access. 2019.
- [5] M. A. S. Masoum and P. S. Moses, "Impact of balanced and unbalanced direct current bias on harmonic distortion generated by asymmetric three-phase three-leg transformers," *IET Electric Power Appl.*, vol. 4, no. 7, pp. 507-515, Aug. 2010.
- [6] G. He, D. Xu and M. Chen, "A novel control strategy of suppressing DC current injection to the grid for single-phase PV inverter," *IEEE Trans. Power Electron.*, vol. 30, no. 3, pp. 1266-1274, Mar. 2015.
- [7] "IEEE Standard for Interconnection and Interoperability of Distributed Energy Resources with Associated Electric Power Systems Interfaces," *IEEE Std 1547-2018*, pp. 1-138, Apr. 2018.
- [8] Y. Yang, K. Zhou and F. Blaabjerg, "Current harmonics from single-phase grid-connected inverters: examination and suppression," *IEEE J. Emerg. Sel. Topics Power Electron.*, vol. 4, no. 1, pp. 221-233, Mar. 2016.
- [9] W. M. Blewitt, D. J. Atkinson, J. Kelly and R. A. Lakin, "Approach to low-cost prevention of DC injection in transformerless grid connected inverters," *IET Power Electron.*, vol. 3, no. 1, pp. 111-119, Jan. 2010.
- [10] N. Mohan, T. Undeland, and W. Robbins, *Power Electronics: Converters, Application and Design*. New York, NY, USA: Wiley, 2002.
- [11] V. Salas, E. Olias, M. Alonso, F. Chenlo, and A. Barrado, "DC current injection into the network from PV grid inverters," in *Proc. IEEE 4th Word Conf. Photovoltaic Energy Convers. Conf. Rec.*, pp. 2371-2374, 2006.
- [12] M. Armstrong, D. J. Atkinson, C. M. Johnson and T. D. Abeyasekera, "Auto-calibrating DC link current sensing technique for transformerless, grid connected, H-bridge inverter systems," *IEEE Trans. Power Electron.*, vol. 21, no. 5, pp. 1385-1393, Sep. 2006.
- [13] Q. Yan, X. Wu, X. Yuan, Y. Geng and Q. Zhang, "Minimization of the DC component in transformerless three-phase grid-connected photovoltaic inverters," *IEEE Trans. Power Electron.*, vol. 30, no. 7, pp. 3984-3997, Jul. 2015.
- [14] R. Sharma, "Removal of DC offset current from transformerless PV inverters connected to unity," in *40th International Universities Power Engineering Conference*, Cork, Ireland, 2005.
- [15] T. Ahföck and L. Bowtell, "DC offset elimination in a single-phase grid-connected photovoltaic system," *Australasian Universities Power Engineering Conference*, Melbourne, Australia, Dec. 10-13, 2006.
- [16] L. Bowtell and A. Ahföck, "Direct current offset controller for transformerless single-phase photovoltaic grid-connected inverters," *IET Renewable Power Generation*, vol. 4, no. 5, pp. 428-437, Sep. 2010.
- [17] S. N. Vukosavić and L. S. Perić, "High-precision active suppression of DC bias in AC grids by grid-connected power converters," *IEEE Trans. Ind. Electron.*, vol. 64, no. 1, pp. 857-865, Jan. 2017.
- [18] G. Buticchi and E. Lorenzani, "Detection method of the DC bias in distribution power transformers," *IEEE Trans. Ind. Electron.*, vol. 60, no. 8, pp. 3539-3549, Aug. 2013.
- [19] M. Chen, D. Xu, T. Zhang, K. Shi, G. He and K. Rajashekara, "A novel DC current injection suppression method for three-phase grid-connected inverter without the isolation transformer," *IEEE Trans. Ind. Electron.*, vol. 65, no. 11, pp. 8656-8666, Nov. 2018.
- [20] W. Zhang, M. Armstrong and M. A. Elgendy, "DC injection suppression in transformer-less grid-connected inverter using a DC-link current sensing and active control approach," *IEEE Trans. Energy Conversion*, vol. 34, no. 1, pp. 396-404, May. 2019.
- [21] A. Abdelhakim, P. Mattavelli, D. Yang and F. Blaabjerg, "Coupled-inductor-based DC current measurement technique for transformerless grid-tied inverters," *IEEE Trans. Power Electron.*, vol. 33, no. 1, pp. 18-23, Jan. 2018.
- [22] Q. N. Trinh, P. Wang, Y. Tang and F. H. Choo, "Mitigation of DC and harmonic currents generated by voltage measurement errors and grid voltage distortions in transformerless grid-connected inverters," *IEEE Trans. Energy Conversion*, vol. 33, no. 2, pp. 801-813, Jun. 2018.
- [23] X. Guo, W. Wu, H. Wu, and G. San, "DC injection control for grid-connected inverters based on virtual capacitor concept," in *Proc. Int. Conf. Elect. Mach. Syst.*, Wuhan, China, pp. 2327-2330, Oct. 2008.
- [24] B. Long, W. Wang, L. J. Huang, Y. Chen, F. S. Li, H. B. Sun and H. Li, "Design and implementation of virtual capacitor based DC current suppression method for grid-connected inverters," *ISA Transactions*, vol. 92, pp. 257-272, 2019.
- [25] B. Long, L. J. Huang, H. B. Sun, Y. Chen F. Victor and K. T. Chong, "An intelligent dc current minimization method for transformerless grid-connected photovoltaic inverters," *ISA Transactions*, vol. 88, pp. 268-279, 2019.
- [26] M. Pahlevani, S. Pan, S. Eren, A. Bakhshai and P. Jain, "An adaptive nonlinear current observer for Boost PFC AC/DC converters," *IEEE Trans. Ind. Electron.*, vol. 61, no. 12, pp. 6720-6729, Dec. 2014.
- [27] Q. N. Trinh, F. H. Choo, Y. Tang and P. Wang, "Control strategy to compensate for current and voltage measurement errors in three-phase PWM rectifiers," *IEEE Trans. Ind. Appl.*, vol. 55, no. 3, pp. 2879-2889, May. 2019.
- [28] Y. Shi, B. Liu and S. Duan, "Eliminating DC current injection in current-transformer-sensed STATCOMs," *IEEE Trans. Power Electron.*, vol. 28, no. 8, pp. 3760-3767, Aug. 2013.
- [29] B. Guo, M. Su, Y. Sun, H. Wang, H. B. Dan, Z. T. Tang, and B. Cheng "A robust second-order sliding mode control for single-phase photovoltaic grid-connected voltage source inverter," *IEEE Access*, vol. 7, pp. 53202-53212, 2019.
- [30] K. Zhou, Y. Yang, F. Blaabjerg and D. Wang, "Optimal selective harmonic control for power harmonics mitigation," *IEEE Trans. Ind. Electron.*, vol. 62, no. 2, pp. 1220-1230, Feb. 2015.
- [31] Y. He, X. Wang, X. Ruan, D. Pan, X. Xu and F. Liu, "Capacitor-current proportional-integral positive feedback active damping for LCL-type grid-connected inverter to achieve high robustness against grid impedance variation," *IEEE Trans. Power Electron.* Early Access, 2019.
- [32] C. Bao, X. Ruan, X. Wang, W. Li, D. Pan and K. Weng "Step-by-step controller design for LCL-type grid-connected inverter with capacitor current feedback active damping," *IEEE Trans. Power Electron.*, vol. 29, no. 3, pp. 1239-1253, Mar. 2014.
- [33] A. G. Yepes, A. Vidal, J. Malvar, O. López and J. Doval-Gandoy, "Tuning method aimed at optimized settling time and overshoot for synchronous proportional-integral current control in electric machines," *IEEE Trans. Power Electron.*, vol. 29, no. 6, pp. 3041-3054, Jun. 2014.
- [34] D. Pan, X. Ruan, X. Wang, H. Yu and Z. Xing, "Analysis and design of current control schemes for LCL-type grid-connected inverter based on a general mathematical model," *IEEE Trans. Power Electron.*, vol. 32, no. 6, pp. 4395-4410, Jun. 2017.
- [35] Y. Xu, Z. Gao and X. Zhu, "Parameter identification of simplified engineering model for PV array based on shuffled frog leaping algorithm," in *20th Int. Conf. Elect. Mach. Syst.(ICEMS)*, Sydney, NSW, pp. 1-6, 2017.
- [36] S. Bacha, I. Munteanu and A. I. Bratcu, "Power electronics converter modeling and control," in *Advanced Textbooks in Control and Signal Processing*, London, U.K.: Springer, 2014.



**Bin Guo** was born in Hubei, China, in 1992. He received the B.S. degrees in electrical engineering from Beihua University, Jilin, China, in 2015. He is currently working toward the Ph.D. degree in the electrical engineering at Central South University, Changsha, China.

His current research interests include modeling and control of power electronics, PV renewable energy and energy storage system, multilevel inverters and soft switch of DC-AC converter.

Mr. Guo is a Frequent Reviewer for the IEEE TRANSACTIONS ON POWER ELECTRONICS, IEEE TRANSACTIONS ON SUSTAINABLE ENERGY, IEEE ACCESS, CSEE JOURNAL OF POWER AND ENERGY SYSTEMS and the *Circuit Word*.



**Mei Su** was born in Hunan, China, in 1967. She received the B.S., M.S. and Ph.D. degrees from Central South University, Changsha, China, in 1989, 1992 and 2005, respectively. Since 2006, she has been a Full Professor with the School of Automation, Central South University.

Her research interests include matrix converter, adjustable speed drives, photovoltaic system and wind conversion system. She is currently an Associate Editor of the IEEE Transactions on Power Electronics.



**Yao Sun** (M'13) was born in Hunan, China, in 1981. He received the B.S., M.S. and Ph.D. degrees from Central South University, Changsha, China, in 2004, 2007 and 2010, respectively. Since 2013, He has been a Full professor with the School of Automation, Central South University.

His research interests include matrix converter, micro-grid and wind energy conversion system.



**Hui Wang** received the B.S., M.S. and Ph.D. degrees from Central South University, Changsha, China, in 2008, 2011 and 2014, respectively. He is currently an associate professor with School of Automation, Central South University.

His research interests include matrix converter, DC/DC converters and solid-state transformer.



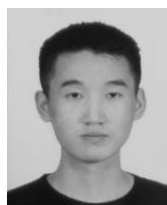
**Xing Li** was born in Hunan, China, in 1988. She received the B.S. and Ph.D. degrees from Central South University, Changsha, China, in 2009 and 2014, respectively. She is currently an Associate Professor with the College of Electrical and Information Engineering, Hunan University, Changsha, China.

Her research interests include power electronic converter and wind energy conversion system.



**Yuefeng Liao** (S' 17) was born in Hunan, China in 1988. He received the B.S. and M.S. degree in control theory and control engineering from Harbin Engineering University, Harbin, China in 2011 and 2013, respectively. He is currently working toward the Ph.D. degree in Central South University.

His research interests include modeling of DC-DC resonant converters, controller design in power electronic and topology research.



**Jianheng Lin** was born in Fujian, China, in 1994. He received the B.S. degree in electronic engineering from Jimei University, Xiamen, China, in 2016. He is currently working toward the Ph.D. degree in control science and engineering at the Central South University, Changsha, China.

His research interests include linear time periodic system analysis and matrix converters.



**Yongheng Yang** (SM'17) received the B.Eng. degree in electrical engineering and automation from Northwestern Polytechnical University, Shaanxi, China, in 2009 and the Ph.D. degree in electrical engineering from Aalborg University, Aalborg, Denmark, in 2014.

He was a postgraduate student with Southeast University, China, from 2009 to 2011. In 2013, he spent three months as a Visiting Scholar at Texas A&M University, USA. Currently, he is an Associate

Professor with the Department of Energy Technology, Aalborg University, where he also serves as the Vice Program Leader for the research program on photovoltaic systems. His current research is on the integration of grid-friendly photovoltaic systems with an emphasis on the power electronics converter design, control, and reliability.

Dr. Yang is the Chair of the IEEE Denmark Section. He serves as an Associate Editor for several prestigious journals, including the IEEE TRANSACTIONS ON INDUSTRIAL ELECTRONICS, the IEEE TRANSACTIONS ON POWER ELECTRONICS, and the IEEE Industry Applications Society (IAS) Publications. He is a Deputy Editor of the IET Renewable Power Generation for Solar Photovoltaic Systems. He was the recipient of the 2018 IET Renewable Power Generation Premium Award and was an Outstanding Reviewer for the IEEE TRANSACTIONS ON POWER ELECTRONICS in 2018.